Materialia 23 (2022) 101444

Contents lists available at ScienceDirect

Materialia

journal homepage: www.elsevier.com/locate/mtla

Fast in-situ synchrotron X-ray imaging of the interfacial reaction during self-propagating exothermic reactive bonding

S. Ramachandran[a], Yi Zhong[b], Stuart Robertson[c], Christoforos Panteli[d], Shuibao Liang[b], Fan Wu[a], Renqian Zhou[a], Shashidhara Marathe[e], Zhaoxia Zhou[c], Andrew S. Holmes[d], Sarah. J. Haigh[a,*], Changqing Liu[b], Wajira Mirihanage[a]

[a] Department of Materials, The University of Manchester, Manchester M13 9PL, UK
[b] Wolfson School of Mechanical, Electrical and Manufacturing Engineering, Loughborough University, Leicestershire LE11 3TU, UK
[c] Loughborough Materials Characterisation Centre, Department of Materials, Loughborough University, Leicestershire LE11 3TU, UK
[d] Department of Electrical and Electronic Engineering, Imperial College London, London SW7 2AZ, UK
[e] Diamond Light Source Ltd, Didcot OX11 0DE, UK

ARTICLE INFO

Keywords:
Self-propagating exothermic reactive (SPER) bonding
Synchrotron in-situ imaging
Wetting
Void formation
quasi ambient bonding (QAB)

ABSTRACT

Self-Propagating Exothermic Reactive (SPER) bonding with lead-free solders is potentially attractive for microelectronics assembly due to its highly localised heating and minimal thermal loading of the components and substrates. The transient dynamics of melting, wetting, solidification and defect formation during SPER bonding were observed using in-situ synchrotron X-ray imaging with sub-millisecond temporal resolution and the results were further analysed using electron microscopy and thermal modelling. In-situ imaging revealed the preferential melting of the solder and subsequent wetting of the substrate. Numerous air bubbles were observed to form at the bonding interface. The distribution of these bubbles was found to vary with the thermal conductivity and wettability of the substrates. These bubbles appear to reduce the effectiveness of bonding by promoting the formation of cracks and voids within the solder joint. Our results show that metallisation layers on the bonding substrate can influence the dynamics of melting for the solder materials and thereby directly influence the reliability of SPER interconnects.

1. Introduction

The evolution of next-generation semiconductors has created opportunities for the miniaturisation of power electronic devices operating at elevated temperatures (above 200°C) [1]. However, conventional soldering techniques generate unwanted thermal damage when seeking to bond high-temperature microelectronic components at high production rates [1]. Environmental and regulatory requirements to move to lead-free solder materials, which typically require higher processing temperatures, are also motivating efforts to develop new integration methods for electronics manufacturing. Self-propagating exothermic reactive (SPER) bonding is an alternative approach which generates minimal thermal effects compared to traditional reflow soldering [2–4]. SPER bonding is performed using multilayer nanofoils consisting of hundreds of alternating metal layers (e.g. Al and Ni with bilayer thickness in the range of 50-200 nm) [5]. Ignition of the nanofoils is typically achieved with an electrical pulse or a laser, causing a self-propagating exothermic reaction that generates instantaneous intense heat [6]. This heat melts the adjacent solder layers, and the subsequent process of interfacial transient wetting and solidification results in metallurgical interconnects. The SPER bonding method has the advantage that quasi-ambient temperature conditions (300 - 400 K) are maintained in the surrounding components [7]. In contrast to traditional soldering processes, SPER bonding with reactive foils usually produces a very high propagation velocity (up to 30 m/s) in the reaction front as well as a high local temperature (>1400°C) within a few milliseconds from the ignition time [8]. This ultrafast reactive bonding technique will result in a sound interfacial bond with minimal thermal effects [4]. The process minimises heat exposure of nearby electronic components which is likely to cause excessive warpage and premature delamination due to high-temperature excursions during electronics manufacturing [9,10]. Consequently, SPER or quasi-ambient bonding has been identified as a promising interconnection technology to enable future sophisticated electronics packaging with minimal adverse heat effects [2–4].

* Corresponding author.
E-mail addresses: sarah.haigh@manchester.ac.uk (S.J. Haigh), C.Liu@lboro.ac.uk (C. Liu), wajira.mirihanage@manchester.ac.uk (W. Mirihanage).

https://doi.org/10.1016/j.mtla.2022.101444
Received 19 April 2022; Accepted 28 April 2022
Available online 29 April 2022

Over the past two decades, the characteristics of SPER bonding have been widely studied [11–18], and a wide range of metals and engineering materials have been successfully joined [11–13]. SPER bonding has also been applied to electronic components, including to bond silicon wafers, and the resultant joints have been characterised to have low thermal resistance and high shear strength [14,15]. Nevertheless, several critical challenges regarding the integrity of SPER bonds need to be addressed before this bonding technology is more widely accepted across the semiconductor industry.

The unacceptably high porosity reported in SPER bonded solder joints is the most severe challenge for their further application since increased porosity tends to be detrimental to reliability [1,19,20]. Both void quantity and void size must meet the standards of the semiconductor industry [21]. Cracks are also commonly observed in SPER joints associated with the nanofoil combustion products and bonding interfaces [1,20]. Studies have suggested that increasing the applied pressure and pre-coating the solder layer on the component surfaces can help to reduce voids [20,22], but this can be difficult to optimise, leading to inconsistent results. It has been shown that the bonding area, solder thickness, and location of nanofoil ignition, all affect crack formation resulting from the volume shrinkage during nanofoil combustion [23,24]. The wetting process is usually recognised as playing the most crucial role in achieving a metallurgical and reliable solder interconnect free from cracks and voids [25], but the very short (millisecond) timescales make it challenging to gain mechanistic insights into this process.

As the SPER process involves a very short cycle time (< 0.1 s) and high heating rates (10^6-10^7 Ks^{-1}) [26], a thorough in-situ characterisation of the diffusion and intermediate phase transformations during the process is crucial for understanding the fast reaction kinetics of the process. In this study, the fast reaction sequences (solidification and wetting) during SPER bonding are investigated by in-situ time-resolved synchrotron X-ray imaging. The melting, void formation, and cracking dynamics were recorded and investigated. This approach enables the real-time observation of the extremely rapid Pb-free solder bonding through the SPER process. The findings from in-situ experiments are analysed and correlated with ex-situ microstructural examinations and thermal modelling. Approaches to reduce voids and cracks during SPER bonding are also discussed based on the new mechanistic knowledge obtained.

2. Experimental methods

2.1. Sample preparation

All nanofoils used in this study were 40 μm thick and contained alternating layers of Al (~60 nm thick) and Ni (~40 nm thick) [24]. Three different multilayer stacking sample configurations were investigated in order to produce an interconnect between a Si component (13.5 mm × 2 mm × 0.4 mm) and an Al substrate (20 mm × 3 mm × 0.5 mm). In sample 1, the behaviour of a stack structure consisting of Si wafer – nanofoil – Al substrate in the absence of solder was studied (referred to as Si-NF-Al). In the sample 2 the nanofoil and a 25 μm thick sheet of solder (SAC 305, with composition 96.5 wt.%Sn-3.0 wt.%Ag- 0.5 wt.%Cu) were sandwiched together to bond the silicon to the Al substrate. SAC is a lead-free alloy commonly used for electronic solders, with a melting point of 217–220°C [27], 34°C higher than a conventional tin-lead (63/37) eutectic alloy solder [28]. The SAC layer is adjacent to the Si, so the complete stack is referred to as Si-SAC-NF-Al. Sample 3 was identical to sample 2 except that the Si substrate was metallised with Ti-Ni-Ag layers (~0.1/1/1 μm thick respectively) to assess if this metallisation improved the quality of the SPER bond, as suggested in previous reports [29]. The complete stack for sample 3 is then Si(Ti/Ni/Ag)-SAC-NF-Al.

2.2. In-situ imaging

In-situ synchrotron X-ray imaging was carried out at the I13-2 beamline of the Diamond Light Source (DLS). A polychromatic X-ray beam

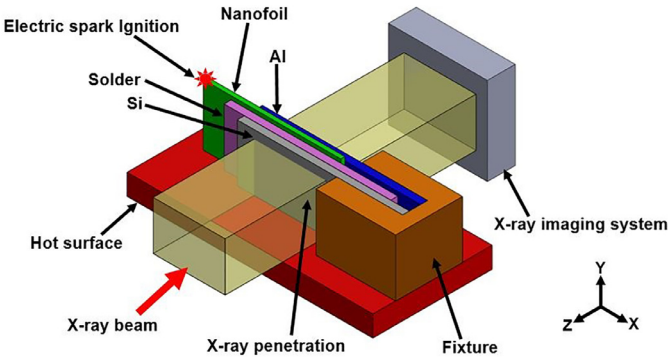

Fig. 1. Schematic representation of the experimental configuration used for high-speed in-situ synchrotron imaging. Specimen shown is sample 2:Si-SAC-NF-Al.

with photon energy centred on 19 keV with ± 5keV weighted mean spectral energy was employed for X-ray transmission imaging of the assembly as shown in Fig. 1, where the imaging optics was placed approximately 0.5 m away from the sample. For image capture, a Pco.Dimax S camera was coupled to a 300 μm LuAG: Ce scintillator using an optical relay system to achieve a ~ 5.5×5.5 mm^2 field of view with 2.75 μm/pixel resolution. The camera was triggered at the maximum 3745 Hz frame rate. This is composed of an exposure time of 0.240 ms and dark time of 0.027 ms giving a total time between recorded frames of 0.267 ms. To reveal the earliest stages of the SPER bonding process, LabVIEW was used to remotely trigger the camera imaging in advance of the pulse signal that produced the nanofoil ignition. The time-resolved image sequences were processed and analysed using ImageJ [30]. An aluminium fixture was used to mechanically support and fix the stack structures to a hot plate for preheating to a temperature of 80°C, monitored by thermocouples. The nanofoil was slightly longer than the neighbouring layers in each case so as to make it accessible for ignition through an electrical ignition probe connected to a direct current power supply of 10 V and 1 A.

2.3. Ex-situ characterisation

For post-reaction microstructural investigations, the 3 samples bonded in the *in*-situ experiments were prepared with a FEI Helios G4 plasma focused ion beam (P-FIB) for SEM analysis. The microstructural analysis was carried out using a field-emission gun scanning electron microscope (SEM) (FEI Helios G4) operated at 5-2 kV and 3.2-0.2 nA.

2.4. Thermal simulations

A three-dimensional finite element model was employed to simulate the effect of the metallisation layer on the solder solidification regime. The thermal transfer behaviour is governed by the equation,

$$\frac{\rho C_P \partial T}{\partial T} + \nabla.(-k\nabla T) = q \ldots\ldots \quad (1)$$

Where T is the temperature, ρ is the density, C_P is the heat capacity, k is the thermal conductivity, q is the heat source that depends on the applied boundary conditions. The heat release from the nanofoil is assumed to be a moving heat source with a velocity of (~12.42 m/s estimated from the experiment, i.e.,

$$q_{NF}(x,t) = Q_s.rect\left(d_n - vt\right) \ldots\ldots \quad (2)$$

where Q_s is the heat released, d_n is the distance of the current position relative to the initial ignition position, and a rectangle function is used to define the size of the heat source zone. More details about the previously validated model can be found in our earlier work [18,31]. Finite element simulations were performed using a time-dependent numerical model based on a simplified description of exothermic reactions through

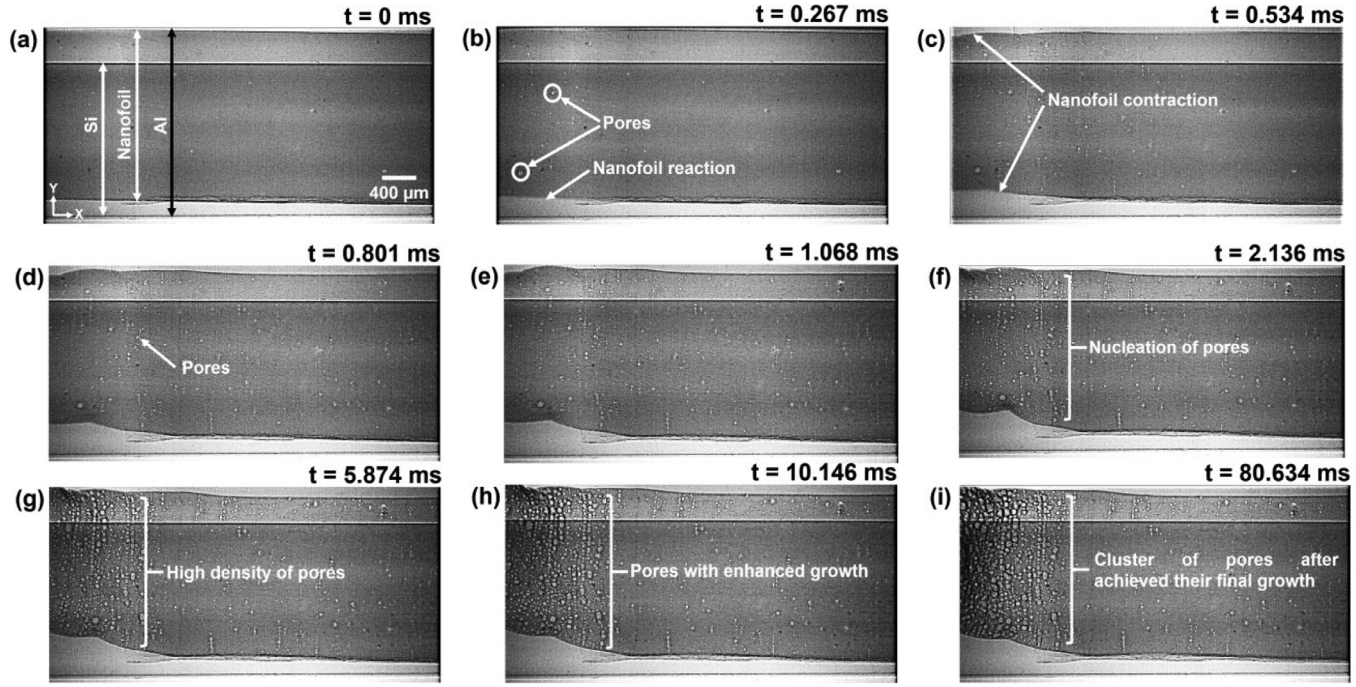

Fig. 2. Time-resolved in situ X-ray transmission radiographs of the Si-NF-Al stack (stack without a solder layer). Note that t=0 ms is the start of the imaging (before the nanofoil ignition). Nanofoil ignition occurs outside the field of view on the left-hand side of the image in the time between t= 0 and t =0.267ms. The stack is clamped outside the field of view on the right-hand side of the image.

the heat-transfer module of COMSOL Multiphysics 5.4. It is known that there are inevitably some air gaps at the contact interface between an electronic device and the heat sink [32], and the low thermal conductivity of air (0.025 W/m•K) [33] can affect the thermal resistance across the Si/solder interface. This can be expected to critically affect the thermal transfer in the stacked interconnects during SPER bonding. Therefore, to analyse the thermal transfer and temperature distribution during bonding two simulation cases were considered with different values of thermal conductance at the Si/solder interface, corresponding to sample 2, the Si-SAC-NF-Al stack, and sample 3, the Si(Ti/Ni/Ag)-SAC-NF-Al stack.

3. In-situ Synchrotron X-ray Imaging Results

3.1. Sample 1: Si-NF-Al

In-situ synchrotron X-ray images of the nanofoil combustion behaviour in the Si-NF-Al stack structure (without solder layer) are shown in Fig. 2. The full video series from which these images are taken can be found in supplementary video 1. The relative alignments of the Si plate, nanofoil, and Al plate are indicated in Fig. 2a, where the different layers of the stack can be distinguished based on their contrast, reflecting the total X-ray transmission of the stack. The X-ray radiograph shown in Fig. 2a (t = 0 ms) is considered as the reference image, representing the start of the imaging prior to the nanofoil ignition. The nanofoil is ignited out of the field of view on the left side of the image area in the period 0<t<0.267ms (between the starting reference frame and the first 'bonding' image). Note that 0.267 ms corresponds to the maximum frame rate of the in-situ camera (3745 Hz). In the first 'bonding' image (t = 0.267 ms), pores start to form and the nanofoil is displaced relative to the reference, as shown in Fig. 2b. By the second bonding image (t = 0.534 ms, Fig. 2c) the contraction of the nanofoil in the Y-direction becomes visible at the top and bottom left of the images on the side where the components are not directly clamped together. The change in the volume ratio between reactants (Ni + Al multilayers in the nanofoils) and combustion product (NiAl intermetallics) can be expected to cause local contraction [34]. Nonetheless, as the contraction in the Y-direction appears first, and is largest, where the nanofoil film is not clamped, it is likely that out-of-plane bending in the imaging direction is the main contributor to this visible contraction (as observed from the perpendicular Z-direction). The observed shrinkage of the nanofoil propagates towards the right-hand side (positive X-direction) as an indicator of the reaction front and completes the entire 4.5 mm length in 1.068 ms (fourth bonding image) giving an estimated propagation rate of 4.21 ± 0.14 m/s, which is slightly slower than that of the free-standing nanofoil reported as ~7.5 - 9.47 m/s [8,26,35]. This decrease in propagation velocity is likely attributed to the bilayer thickness of the nanofoil [36] and the heat transfer characteristics of the encapsulating materials [8,35].

Analysis of subsequent images later in the time series shows that the unclamped side of the nanofoil continued to deform until 80.634 ms (Fig. 2i), after which no obvious changes were observed (see supplementary video 1). The large contraction in the Y-direction, likely resulting from the out-of-plane bending, together with the large distortion of the layer position in the Y-direction and absence of visible cracking, suggests that the nanofoil is relatively ductile behind the reaction front, in agreement with previous findings [26,37]. The contraction of the foil along Y is accompanied by the formation of pores in the nanofoil, first observed at the earliest stages of the reaction (first bonding image, Fig. 2b, 0.267ms). These pores nucleate and grow over time and at 2.136 ms (8th bonding image) many spherical pores, likely containing the partitioned gases from the solidifying melt, with sizes of 10-100 μm are clearly visible. Gases may result from those dissolved in the liquid metal and evolved as the metal solidifies or due to heat-induced expansion of air pockets trapped at the interface. The highest bubble density was seen at the unclamped (negative X) end with a tendency to align in strips perpendicular to the nanofoil propagation direction (Fig. 2f). After 80 ms, many pores with diameters of >100 μm dominate the morphology of the film at the unclamped end and are also present in smaller numbers and with smaller diameters on the clamped right-hand side (Fig. 2i).

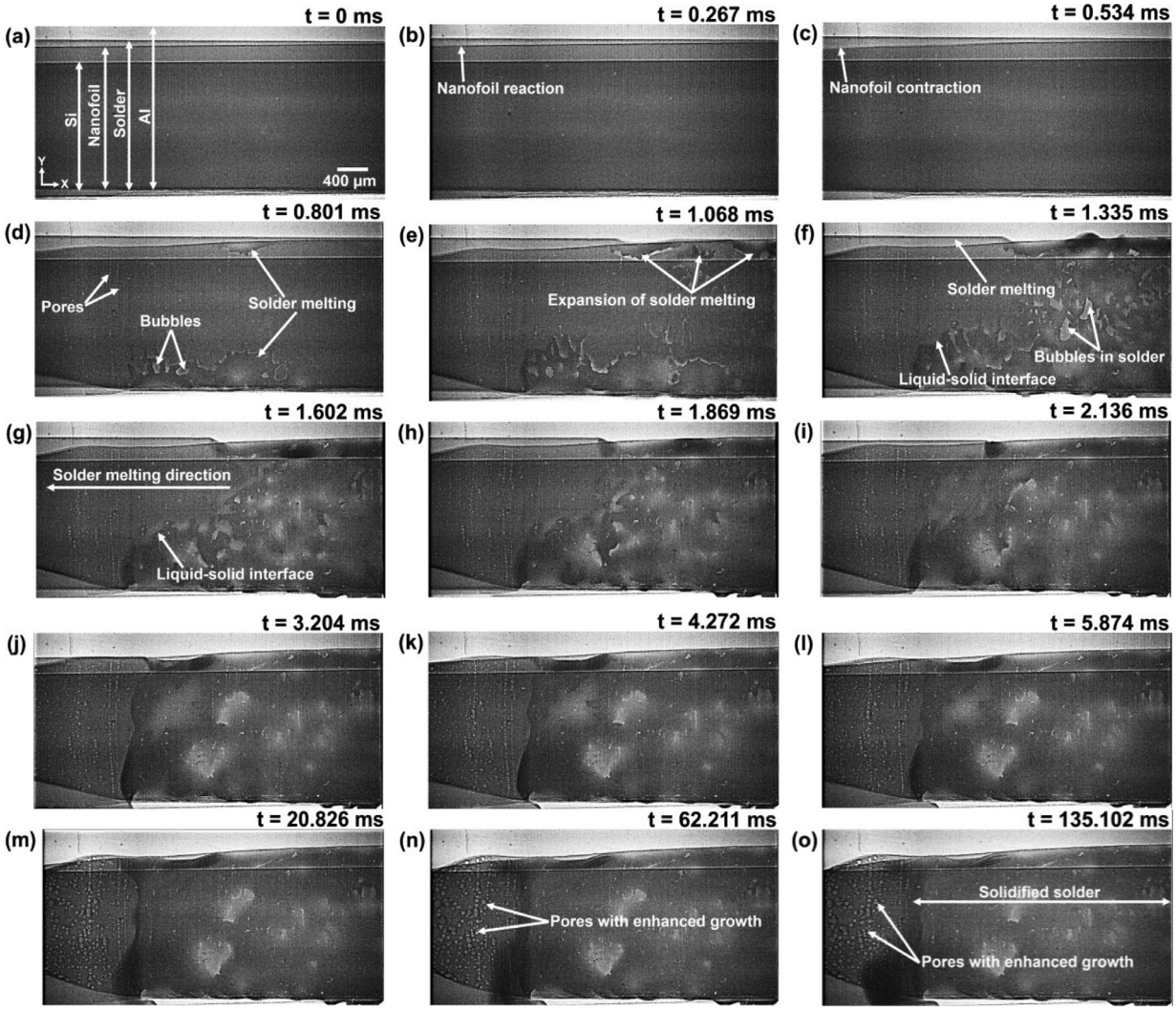

Fig. 3. Time-resolved in-situ X-ray radiographs of the Si-SAC-NF-Al stack (multilayer stacking system with a solder layer but without metallisation on the Si substrate). Similar to Figure 2 nanofoil ignition occurs outside the field of view on the left-hand side of the image between t = 0 and t = 0.267ms. The stack is clamped outside the field of view on the right-hand side of the image.

3.2. Sample 2: Si-SAC-NF-Al

Selected X-ray transmission images from the in-situ synchrotron experiment for SPER bonding of the Si-SAC-NF-Al stack, are shown in Fig. 3. The full video series from which these images are taken can be found in supplementary video 2. The relative locations of the Si plate, nanofoil, SAC solder layer, and Al plate are indicated in the reference image at t=0 (Fig. 3a). A dynamic response from the stack is observed in the first image after ignition (Fig. 3b), at t = 0.267 ms, where shrinkage in the Y-direction is evidence of the nanofoil reaction. The reaction front is seen to have propagated across the full 4.5 mm field of view within 1 frame (0.267 ms) giving a velocity of >12.42 m/s, although we note this is a lower limit since observing a higher propagation rate for the same field of view would require a faster imaging speed than is achievable with the in-situ camera. This is faster than the speed for the nanofoil stack without SAC (4.21 m/s) and also faster than the rate reported previously for nanofoils coated with just a 1 μm Incusil solder layer (7.6 m/s) [38]. Fig. 3c-f show further shrinkage of the nanofoil, reaching ~7% of the projected width. In the third bonding image, at t = 0.801 ms, a mottling becomes visible in the edges of the sample (Fig. 3d), which is indicative of local melting of the solder. Lower intensity, mobile, spherical features are also visible in this region, suggesting voids or air bubbles in the specimen, which locally decrease the thickness and increase X-ray penetration. These bubbles are likely to be caused by thermal expansion of air, expected to be trapped at the stacking interfaces as a result of inhomogeneous contact. At 1.335 ms (fifth bonding image, Fig. 3f), the molten solder regions at the edges of the film combine and the total molten area continues to propagate towards the unclamped left-hand side, as shown in Fig. 3f-j.

From Fig. 3g-j, it is noticed that the rapid heat produced by the reactive nanofoil progressively melts the solder layer, leading to a melting front that propagates away from the clamp. After 3.204 ms (Fig. 3j), there is no significant change in the area of solder melt indicating that the solder in contact with the nanofoil was fully molten within ~3 ms. The video captured for 4.272-20.826 ms shows evidence of the movement and agglomeration of air bubbles in the solder region, demonstrating that the solder remains liquid for approximately 20 ms (see supplementary video 2) . Image frames from 20.826-62.211 ms show no further bubble motion, but a sudden shrinkage of the solder melt is observed, likely due to the contraction of the molten solder caused by cooling. Some density variations remain even in the fully cooled joined specimen.

Importantly, pores similar in appearance to those observed in Fig 2 (see supplementary video 2) are visible in the nanofoil on the left-hand side where the solder layer does not melt, but not in the region where the molten solder appears. These pores grow during the later

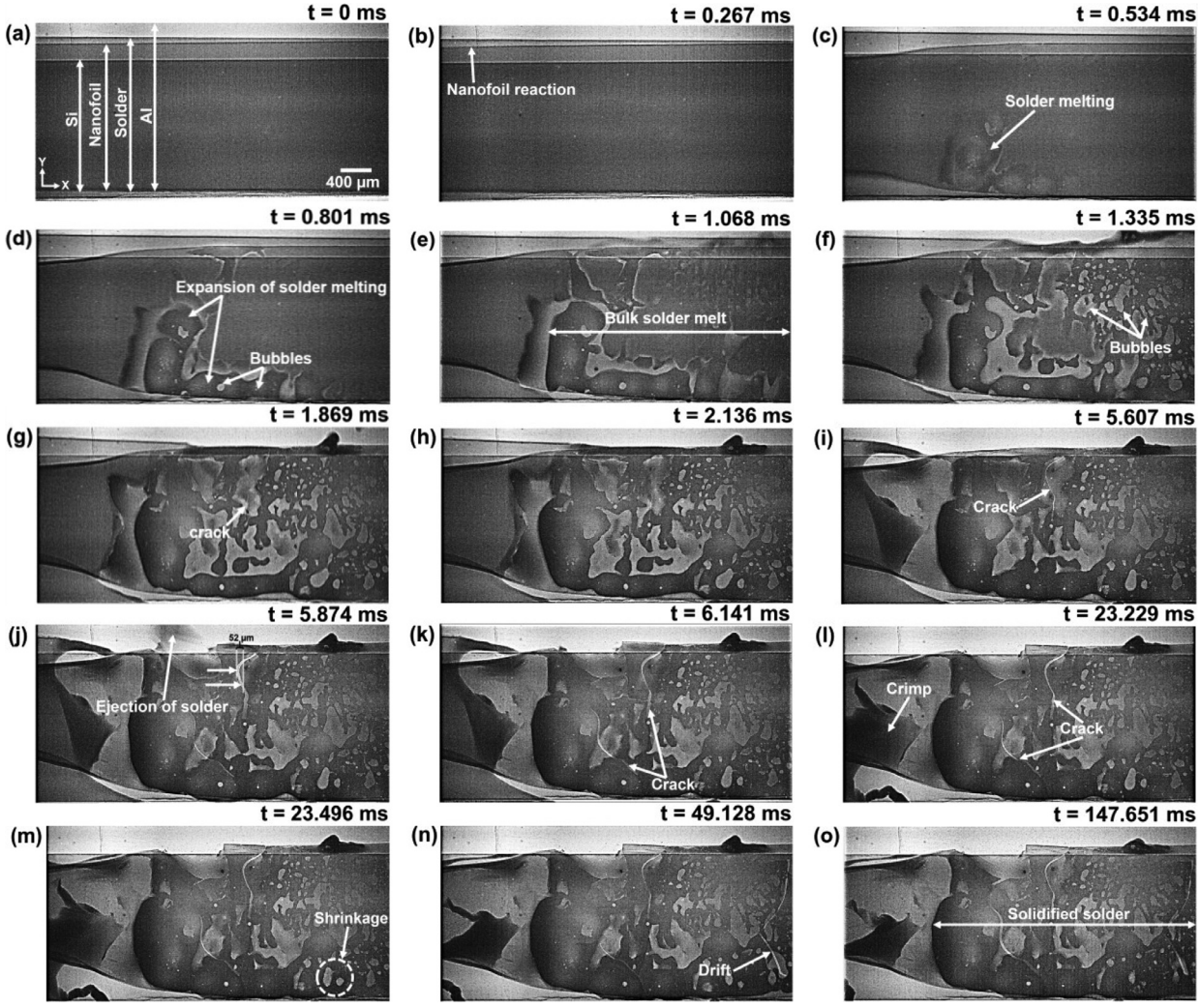

Fig. 4. Time-resolved in-situ X-ray radiographs of the Si(Ti/Ni/Ag)-SAC-NF-Al stack (multilayer stacking system with a solder layer and also with the Ti/Ni/Ag metallisation on the Si substrate). Similar to Fig. 3 nanofoil ignition occurs outside the field of view on the left-hand side of the image between t = 0 and t = 0.267ms. The stack is clamped outside the field of view on the right-hand side of the image.

video frames in a similar fashion to that discussed in Fig 2. The observation that where the solder melts no pores are visible suggests that the generation of molten solder during the bonding reaction is key to filling of pores in the nanofoil.

3.3. Sample 3: Si(Ti/Ni/Ag)-SAC-NF-Al

Fig. 4 shows selected images from the in-situ synchrotron video sequence of the Si(Ti/Ni/Ag)-SAC-NF-Al stack (for full sequence, see supplementary video 3). The relative locations of the Si die, Nanofoil, SAC solder layer, and Al plate are indicated on the reference image (Fig. 4a). As for previous stacks, the start of the nanofoil reaction is visible by a slight contraction of the nanofoil in the first bonding image at 0.267 ms (Fig. 4b). In the second bonding image, at 0.534 ms, a mottled patch becomes visible at the bottom edge and centre-left regions, indicating solder melting. This provides indirect evidence that the nanofoil reaction front propagation speed is similar to that seen in the Si-SAC-NF-Al stack, with the reaction being completed in the first 0.8 ms. By the fourth bonding image, t=1.068 ms, the area of molten solder has expanded over the entire X-ray inspected area in the stack as mottling appears in the right-hand side of the image (Fig. 4e). At this point in the reaction, bright bubble-like features are visible in the centre of the stack, with these features appearing over the whole molten area by the fifth bonding image (t=1.335 ms, Fig. 4f). Most of these relatively low-density regions are mobile and have sharp boundaries, with sizes ranging from microns to millimetres, suggesting they are air bubbles trapped at the interfaces. Interestingly the reaction appears more violent than sample 2 (the identical geometry but without metallisation), with SAC melting the top and bottom of the image in the clamped region of the stack accompanying the nanofoil reaction in the first ~1 ms (Fig. 4e).

In the time series images from 1-13 ms (see supplementary video 3), the solder layer on the unclamped left-hand side of the sample also melts. This contrasts to the stack without Si metallisation (Fig. 3, supplementary video 2), where the SAC solder in the unclamped end of the stack did not melt during the reaction. Later images, from t=13 ms to the end of the reaction show that the SAC in the unclamped region solidifies in inhomogenous patches with a part hanging free and large areas of this region having low intensity, suggesting there is little SAC remaining. We will thus focus further discussion on the behaviour of the clamped right-hand side, as this area is more representative of a successful joint.

After initial melting, the SAC layer in sample 3 can be separated into three regions with different characteristic appearances. These are proposed to correspond to solid SAC (low intensity, abrupt edges, immo-

bile), molten SAC (low intensity, soft edges, mobile) and bubbles (high intensity); see supplementary video 3 for evidence of mobility. At 1.869 ms a crack appears in the centre of the stack, as indicated on Fig. 4g. As the accompanying video suggests that the SAC remains fully molten in this region the crack is likely associated with the reacted nanofoil, due to the internal stress resulting from the out-of-plane bending in the unclamped left-hand side. Even after the SAC has melted across the whole X-ray detected region, structural inhomogeneity and the likely accompanying temperature variations continue to cause violent evolution in the clamped region. The temperature increase of trapped air bubbles will be slower than the surrounding materials due to the poor thermal conductivity of air (~0.025 W/m•K), which is several orders of magnitude smaller than that of metals (e.g. ~32.5 W/m•K for molten tin [39]). In addition, with the limited heat dissipation of the solder layer, the heat released in the exothermic reaction (~4.54×10^8 W/cm^3) [18] causes a prolonged temperature differential between the solder and the nanofoil [17]. The evidence of the thermal stresses present in the stack is observable by the abrupt ejection of a solder droplet from the top of the sample at t = 5.874 ms, when a bubble appears to burst out from the interface (Fig. 4j). A droplet is launched out of the stack and travels ~0.43 mm within one frame (0.267 ms), giving an initial velocity of the droplet more than 1.40 m/s. The expulsion event is closely followed by widespread cracking across the whole width of the stack in both the nanofoil and the SAC layer as highlighted on Fig. 4k. This includes significant enlargement of the crack earlier identified in the nanofoil. Such expulsion of material is also very undesirable for microelectronic bonding applications as solder may splash on to nearby components potentially causing unwanted conductive paths.

The next 45 ms (to t = 48.861 ms)are accompanied by slow expansion of the solidified areas and many smaller cracks appearing in the centre of the stack which has the lowest density (suggesting the biggest local loss of SAC volume). Drifting of bubbles within the darker solidified areas suggests interfacial liquid remains present. At 23.229-23.496 ms, a crimping of the solder in the unclamped region is accompanied by significant lateral motion of material in the lower part of the clamped region, probably resulting from an abrupt volume contraction during cooling. At 49.128 ms a crack appears in the nanofoil, dissecting almost the full width on the right-hand side of the stack. Its presence causes a bubble to appear in the solder for the whole length of the crack as well as significant local movement of existing bubbles. This suggests that at 49 ms the majority of the SAC layer is still in liquid or semi-solid state which is readily deformed. The later stages of cooling and solidification up to t= 159 ms show comparatively minor visible changes, confined to the movement of interfacial bubbles (see supplementary video 3). This value is much longer than the total duration of solder melting reported in existing reactive bonding studies attempted through numerical analysis on different stacking materials and bonding conditions [17,40], which did not consider the interfacial thermal resistance and the undercooling in solidification. Importantly the presence of bubbles moving independently in different directions within the same specimen area suggests that they are present on at least two different internal interfaces. The final morphology of the stack contains many large cracks (10s μm wide and mm in length) as well as large bubble features and patches of low contrast suggesting the absence of SAC layer.

4. Analysis and microstructural characterisation

4.1. Solder melting and solidification rates

Previous experiments [41,42] have reported that the undercooling of Pb-free solders can reach up to 90°C although this varies with the size, substrate and cooling conditions. The thin nanofoils used in SPER bonding provide a fixed amount of heat; however, the duration for which the solder remains in a molten state will be affected by the contact to the nanofoil, ambient conditions and the physical properties of solder layers and surrounding components (e.g., thermal capacity and conductivity). The projected area of molten solder for the Si-SAC-NF-Al and Si(Ti/Ni/Ag)-SAC-NF-Al stacks was measured as a function of time, as shown Fig. 5. It is interesting to note that the SAC in the metallised stack (Si (Ti/Ni/Ag)-SAC-NF-Al, Fig. 4) appears to melt slightly more quickly and more completely than in the Si-SAC-NF-Al stack (Fig. 3). Key points in the reactions are indicated on the graph, with numbers 1-3 showing the nanofoil ignition, bulk solder melting, and complete melting of the whole X-ray inspection region, respectively. It should be noted that in both cases the nanofoil reaction was complete within ~2 ms, so after this point the heat being applied to the SAC is expected to be decreasing.

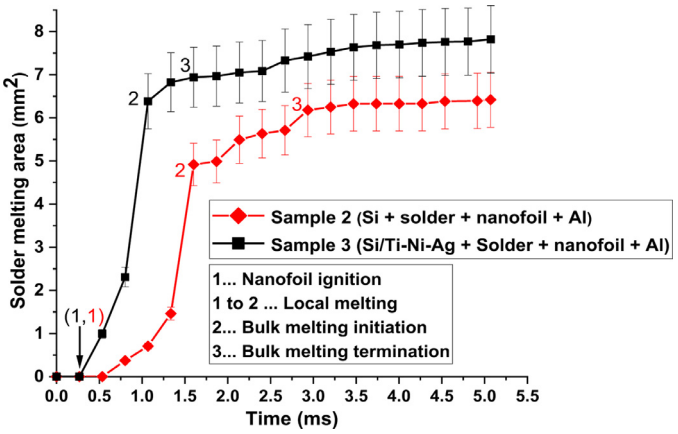

Fig. 5. Evolution of the solder melting area with time for samples 2 and 3.

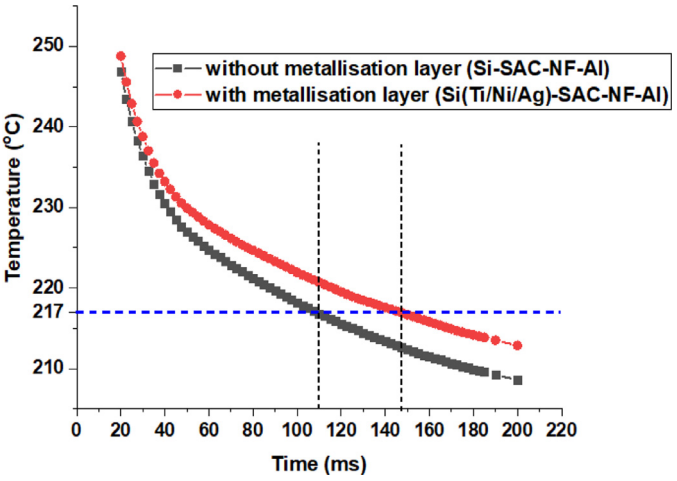

Fig. 6. Numerical simulation of the time versus temperature profile of the SAC solder (with and without metallised layer on the Si substrate), where the blue dotted line denotes the melting point of the solder.

The observed difference between the metallised and the bare Si substrate can be explained based on the thermal properties of the stack (especially the coefficient of thermal expansion and thermal conductivity). For the Si(Ti/Ni/Sg)-SAC-NF-Al stack, the metallised layer (Ti/Ni/Ag) would significantly alter the heat transfer during the bonding process. Fig. 6 presents the simulated temperature profiles of the point at the mid-layer of the SAC solder during SPER bonding for the two cases. The presence of the metallisation layer is found to slow the heat transfer, leading to high temperatures being retained in the early stages of the reaction, and thus producing the faster melting of the solder that we observe experimentally. Although faster melting might be considered to be a favourable feature of a bonding reaction, our in-situ data demonstrates this is accompanied by explosive expulsion of solder from

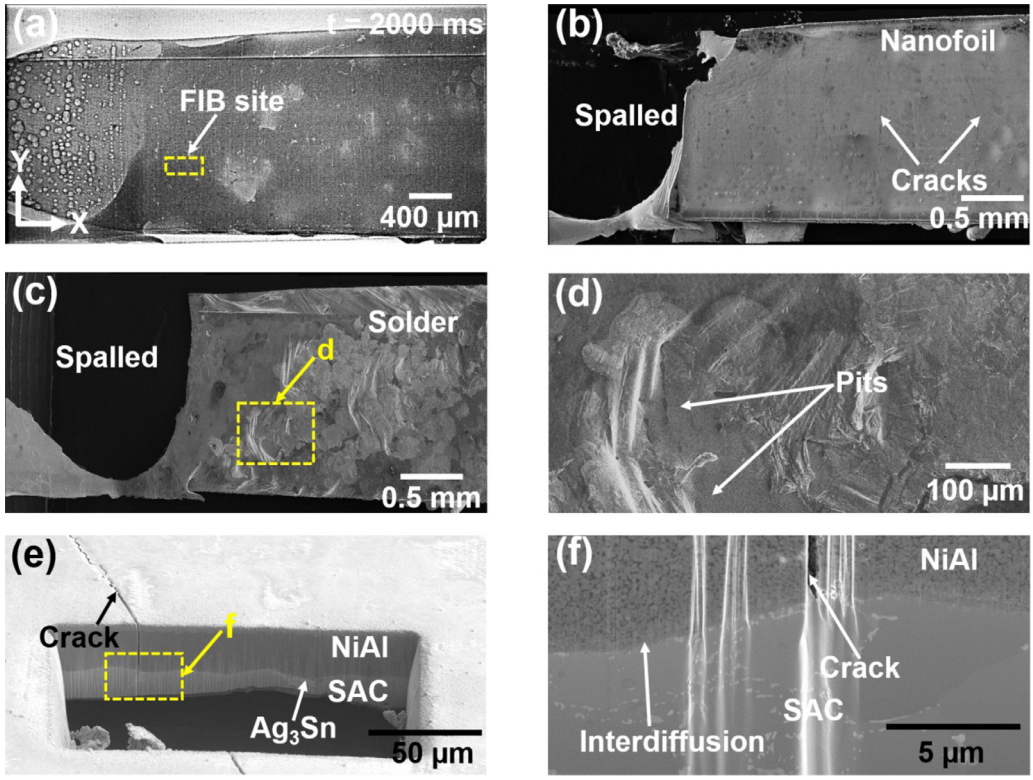

Fig. 7. Comparison of ex-situ SEM microstructural analysis of the Si-SAC-NF-Al stack with the in-situ images: (a) The in-situ X-ray radiograph captured at 2000 ms (after completion of the reaction), (b) Top-view of the nanofoil (NiAl) side of the sample, (c) Top-view of the solder (SAC) side of the sample, (d) Magnified image of the region shown in (c), (e) SEM image of the FIB milled cross-section through a crack feature, (f) Magnified cross-sectional view of the region shown in (e).

interfaces, cracking and large inhomogeneities in the resulting solder distribution. The slower cooling predicted by the simulation results in Fig. 6 also means that the temperature of the SAC layer remains above the melting temperature for longer with metallisation (~144 ms for the Si(Ti/Ni/Sg)-SAC-NF-Al stack but ~110ms for the Si-SAC-NF-Al stack). This is consistent with our experimental observations of more complete solder melting in the metallised stack, even persisting to where the solder and the nanofoil are unclamped. Again, although complete melting is beneficial, this slow cooling could also have a negative impact on the bond integrity. Relatively longer time in the molten state or relatively slower cooling times are known to significantly increase the likelihood of reaction between the solder and the air as well for air to be trapped within the joint [43].

4.2. Defect formation

The Al plate was removed from the Si-SAC-NF-Al stack and Si(Ti-Ni-Ag)-SAC-NF-Al stacks (samples 2 and 3) in order to facilitate ex-situ microstructural characterisation. The surface morphology of the nanofoil side of the in-situ reacted nanofoil-SAC solder sample 2(Si-SAC-NF-Al stack) is shown in Fig. 7(b). This secondary electron SEM image has been flipped to match the geometry of the in-situ X-ray images from Fig. 3, with the final image in the in-situ movie shown in Fig. 7(a) for reference. Several cracks are visible in the reacted nanofoil, mainly oriented along the Y-direction, as indicated in Fig. 7(b), although no cracking was observed in the synchrotron images. This is potentially due to the limited pixel size of the X-ray images which is larger than the width of the cracks. The SEM images in Fig. 7(c) and Fig. 7(d)) show the surface morphology of the SAC solder side of the extracted SAC-nanofoil sample. Fig. 7(d) demonstrates the presence of large pits at the regions of lower density observed in the synchrotron X-ray image (Fig. 7a). These pits mean that the SAC solder layer is thinner, causing the observed higher intensity in the corresponding X-ray transmission image, and could be associated with a region of local porosity at the SAC-Si interface. Fig. 7e and f show a cross-section extracted by FIB milling from the bonded nanofoil/solder at the location marked in Fig. 7a where there is a crack in the nanofoil. Fig. 7e shows the cross-sectional morphology demonstrating that the crack is not filled by solder. Thus, the crack is likely initiated by the thermal stress during a later cooling stage as a result of higher thermal gradients and differences in thermal expansion coefficient (CTE) between the SAC (22.9×10^{-6} K^{-1}) [44] and the NiAl intermetallic produced by the nanofoil reaction (14×10^{-6} K^{-1}) [45]. Fig. 7f shows the magnified image of the location mapped in Fig. 7e, where the Ag_3Sn interdiffusion layer is evident between the SAC and NiAl, and the image reveals that the crack propagated into the interdiffusion layer but not into the bulk of the SAC.

Fig. 8 shows similar SEM microstructural analysis of the Si(Ti-Ni-Ag)-SAC-NF-Al stack after in-situ imaging. The SEM image of the nanofoil side of the nanofoil-SAC stack (after removing the Al plate) is shown in Fig. 8(b), with the image Fig. 8(a) duplicated for ease of comparison to the in-situ X-ray images in Fig. 4. Large cracks with big intersection angles are observed in the NiAl intermetallic, and the crack locations agree well with those visible in the in-situ X-ray images. Vertical cracks in the brittle NiAl layer are commonly observed in SPER bonded solder joints [46]. Fig 8c shows the formation of an intermetallic layer at the interface between NiAl and SAC. This intermetallic layer is Ag_3Sn [18], and is also visible in the magnified image, in Fig 8d. In addition, large bubble voids in the SAC solder (>10µm in diameter) can be observed in Fig. 8(c) and (d), at a position that agrees well with the low-density region seen in the in-situ X-ray transmission results. The cross-sectional morphology close to a crack in the NiAl layer is shown in Fig. 8(e) and (f), where it can be seen to be partly filled by the SAC solder, which indicated the crack initiated before complete solder solidification. These figures confirm that when cracks form before the end of SAC

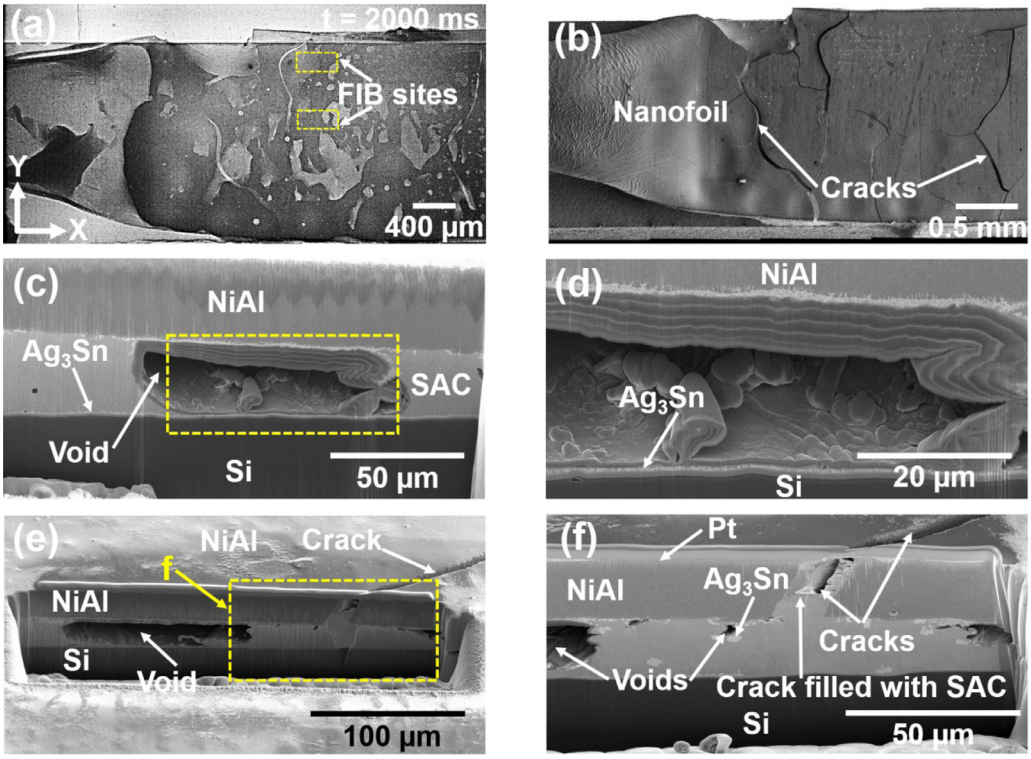

Fig. 8. Comparison of ex-situ SEM microstructural analysis of the Si(Ti/Ni/Ag)-SAC-NF-Al stack with in-situ X-ray data: (a) The in-situ X-ray radiograph captured at 2000 ms (after completion of reaction dynamics), (b) Top-view of the NiAl layer of the bonded stack, (c) Cross-sectional SEM image after FIB milling through the SAC layer, (d) Magnified image of the region shown in (c), (e) Morphology of crack and void, (f) Magnified image of the region located in (e).

solidification they can be filled by solder, whereas cracking after solidification results in unfilled cracks in the nanofoil as observed in the Si-SAC-NF-Al stack.

5. Conclusions

We have successfully applied in-situ X-ray imaging to the real-time observation of melting, wetting, void formation and cracking during SPER bond formation with < 0.5 ms temporal and <10 μm spatial resolutions. Coupled with thermal simulations and ex-situ microstructural characterisation, the results demonstrate new insights into the SPER bonding process which can be applied to develop new bonding approaches with reduced defects and improved bond strength. The main contributions of this article are (1) revealing the void formation mechanisms, and (2) demonstrating the influence of the substrate on the reliability of SPER interconnects. More specifically, this work:

- Demonstrates the use of in-situ X-ray imaging to reveal time-resolved information on void formation processes and their relationship to the bond components.
- Demonstrates that the metallised layer on the Si substate significantly slows the heat transfer away from the nanofoil, causing faster and more complete melting of the solder, but also resulting in the molten solder phase existing for a longer time. This is shown to induce dynamic stresses, likely due to trapped air at the interfaces and consequently has a negative impact on bond integrity, leading to cracking and porosity. A faster cooling rate when the metallisation layer is absent results in a bond with fewer, smaller cracks and a more homogeneous solder layer.
- Nonetheless it is shown that achieving bond integrity requires sufficient heat retention to ensure full melting of the solder, since in the absence of solder the reacted nanofoil contains a high concentration of linear pore features, especially in the absence of local physical clamping. This motivates the further investigation of the optimal heat transfer for different bond geometries to ensure complete solder melting together with rapid cooling to minimise defect formation.

Declaration of Competing Interest

The authors declare that they have no known competing financial interests or personal relationships that could have appeared to influence the work reported in this paper.

Acknowledgements

This research was supported by the EPSRC research grants (Grant No. EP/R031711/1, EP/R031770/1, and EP/R032203/1). The authors would like to thank the Indium Corporation (USA) and Dynex Semiconductor Ltd (UK) for supplying nanofoils and Si dies, respectively. Diamond Light Source is acknowledged for granting beam time to undertake the experiments at beamline I13-2 (MG24151). The authors also acknowledge use of facilities within the Loughborough Materials Characterization Centre and for access to the Helios PFIB, funded by the EPSRC grant EP/P030599/1 and also use of electron microscopy facilities in the Henry Royce Institute for Advanced Materials (funded through EP/R00661X/1, EP/S019367/1, EP/P025021/1 and EP/P025498/1).

Supplementary materials

Supplementary material associated with this article can be found, in the online version, at doi:10.1016/j.mtla.2022.101444.

References

[1] Y. Zhong, A.Y. Liu, S. Robertson, S. Liang, Z. Zhou, C. Liu, Quasi-ambient Bonding Semiconductor Components for Power Electronics Integration, in: 2020 IEEE 70th Electron. Components Technol. Conf., 2020, pp. 1468–1473, doi:10.1109/ECTC32862.2020.00232.

[2] F. Baras, O. Politano, Epitaxial growth of the intermetallic compound NiAl on low-index Ni surfaces in Ni/Al reactive multilayer nanofoils, Acta Mater 148 (2018) 133–146, doi:10.1016/j.actamat.2018.01.035.

[3] M. Mueller, J. Franke, Highly efficient packaging processes by reactive multilayer materials for die-attach in power electronic applications, in: 2014 IEEE 16th Electron. Packag. Technol. Conf., 2014, pp. 477–481, doi:10.1109/EPTC.2014.7028295.

[4] X. Wang, M. Li, W. Zhu, Formation and homogenization of Si interconnects by non-equilibrium self-propagating exothermic reaction, J. Alloys Compd. 817 (2020) 153210, doi:10.1016/J.JALLCOM.2019.153210.

[5] K. Maekawa, K. Kodama, S. Miyake, T. Namazu, Laser-induced multiple points ignition test in Al/Ni exothermic reactive film for crack propagation control, Jpn. J. Appl. Phys. 60 (2021) SCCL15, doi:10.35848/1347-4065/abf39c.

[6] F. Baras, V. Turlo, O. Politano, S.G. Vadchenko, A.S. Rogachev, A.S. Mukasyan, SHS in Ni/Al Nanofoils: A Review of Experiments and Molecular Dynamics Simulations, Adv. Eng. Mater. 20 (2018) 1800091, doi:10.1002/adem.201800091.

[7] A.S. Rogachev, Exothermic reaction waves in multilayer nanofilms, Russ. Chem. Rev. 77 (2008) 21–37, doi:10.1070/rc2008v077n01abeh003748.

[8] Z. Zhou, L. Mo, H. Liu, Y.C. Chan, F. Wu, Study of Fusion Thickness of Tin Solder Heating by Self-Propagating Exothermic Reaction, J. Electron. Mater. 47 (2018) 7435–7448, doi:10.1007/s11664-018-6684-9.

[9] R. Khazaka, L. Mendizabal, D. Henry, R. Hanna, Survey of High-Temperature Reliability of Power Electronics Packaging Components, IEEE Trans. Power Electron. 30 (2015) 2456–2464, doi:10.1109/TPEL.2014.2357836.

[10] S. Zhang, H. Yang, K. Gao, L. Yan, X. Pang, A.A. Volinsky, Residual stress and warpage of AMB ceramic substrate studied by finite element simulations, Microelectron. Reliab. 98 (2019) 49–55, doi:10.1016/j.microrel.2019.04.025.

[11] D.P. Adams, Reactive multilayers fabricated by vapor deposition: A critical review, Thin Solid Films 576 (2015) 98–128, doi:10.1016/j.tsf.2014.09.042.

[12] A.J. Swiston, E. Besnoin, A. Duckham, O.M. Knio, T.P. Weihs, T.C. Hufnagel, Thermal and microstructural effects of welding metallic glasses by self-propagating reactions in multilayer foils, Acta Mater 53 (2005) 3713–3719, doi:10.1016/j.actamat.2005.04.030.

[13] D. Bridges, C. Rouleau, Z. Gosser, C. Smith, Z. Zhang, K. Hong, J. Cheng, Y. Bar-Cohen, A. Hu, Self-Powered Fast Brazing of Ti-6Al-4V Using Ni/Al Reactive Multilayer Films, Appl. Sci. 8 (2018), doi:10.3390/app8060985.

[14] J. Braeuer, T. Gessner, A hermetic and room-temperature wafer bonding technique based on integrated reactive multilayer systems, J. Micromechanics Microengineering. 24 (2014) 115002, doi:10.1088/0960-1317/24/11/115002.

[15] S. Miyake, S. Kanetsuki, K. Morino, J. Kuroishi, T. Namazu, Thermal property measurement of solder joints fabricated by self-propagating exothermic reaction in Al/Ni multilayer film, Jpn. J. Appl. Phys. 54 (2015) 06FP15, doi:10.7567/jjap.54.06fp15.

[16] S. Jayaraman, A.B. Mann, M. Reiss, T.P. Weihs, O.M. Knio, Numerical study of the effect of heat losses on self-propagating reactions in multilayer foils, Combust. Flame. 124 (2001) 178–194, doi:10.1016/S0010-2180(00)00192-9.

[17] J. Wang, E. Besnoin, O.M. Knio, T.P. Weihs, Effects of physical properties of components on reactive nanolayer joining, J. Appl. Phys. 97 (2005) 114307, doi:10.1063/1.1915540.

[18] W. Zhu, X. Wang, C. Liu, Z. Zhou, F. Wu, Formation and homogenisation of SnCu interconnects by self-propagated exothermic reactive bonding, Mater. Des. 174 (2019) 107781, doi:10.1016/j.matdes.2019.107781.

[19] B. Boettge, J. Braeuer, M. Wiemer, M. Petzold, J. Bagdahn, T. Gessner, Fabrication and characterization of reactive nanoscale multilayer systems for low-temperature bonding in microsystem technology, J. Micromechanics Microengineering. 20 (2010) 64018, doi:10.1088/0960-1317/20/6/064018.

[20] W. Zhu, Soldering Interconnects Through Selfpropagating Reaction Process, Loughborough University, 2016 https://hdl.handle.net/2134/23259.

[21] E. Padilla, V. Jakkali, L. Jiang, N. Chawla, Quantifying the effect of porosity on the evolution of deformation and damage in Sn-based solder joints by X-ray microtomography and microstructure-based finite element modeling, Acta Mater 60 (2012) 4017–4026, doi:10.1016/j.actamat.2012.03.048.

[22] J. Wang, E. Besnoin, O.M. Knio, T.P. Weihs, Investigating the effect of applied pressure on reactive multilayer foil joining, Acta Mater 52 (2004) 5265–5274, doi:10.1016/j.actamat.2004.07.012.

[23] T. Namazu, K. Ohtani, K. Yoshiki, S. Inoue, Crack propagation direction control for crack-less solder bonding using Al/Ni flash heating technique, in: 2011 16th Int. Solid-State Sensors, Actuators Microsystems Conf., 2011, pp. 1368–1371, doi:10.1109/TRANSDUCERS.2011.5969524.

[24] K. Maekawa, S. Ito, T. Namazu, Influence of bonded area size on cracking in reacted NiAl layer for crack-free reactive soldering, Jpn. J. Appl. Phys. 59 (2020) SIIL01, doi:10.35848/1347-4065/ab769b.

[25] T. Matsumoto, K. Nogi, Wetting in Soldering and Microelectronics, Annu. Rev. Mater. Res. 38 (2008) 251–273, doi:10.1146/annurev.matsci.38.060407.132448.

[26] A.S. Rogachev, S.G. Vadchenko, A.S. Mukasyan, Self-sustained waves of exothermic dissolution in reactive multilayer nano-foils, Appl. Phys. Lett. 101 (2012) 63119, doi:10.1063/1.4745201.

[27] Z. Zhou, A. Zhang, X. Guan, H. Liu, C. Liu, F. Wu, Microstructural and Micromechanical Characteristics of Tin-Based Solders Under Self-Propagating Exothermic Reaction Heating, J. Electron. Mater. 49 (2020) 6214–6222, doi:10.1007/s11664-020-08363-9.

[28] M.A. Fazal, N.K. Liyana, S. Rubaiee, A. Anas, A critical review on performance, microstructure and corrosion resistance of Pb-free solders, Measurement 134 (2019) 897–907, doi:10.1016/j.measurement.2018.12.051.

[29] H.R. Kotadia, P.D. Howes, S.H. Mannan, A review: On the development of low melting temperature Pb-free solders, Microelectron. Reliab. 54 (2014) 1253–1273, doi:10.1016/j.microrel.2014.02.025.

[30] C.A. Schneider, W.S. Rasband, K.W. Eliceiri, NIH Image to ImageJ: 25 years of image analysis, Nat. Methods. 9 (2012) 671–675, doi:10.1038/nmeth.2089.

[31] S. Liang, Y. Zhong, S. Robertson, A. Liu, Z. Zhou, C. Liu, Investigation of Thermo-mechanical and Phase-change Behavior in the Sn/Cu Interconnects during Self-Propagating Exothermic Reaction Bonding, in: 2020 IEEE 70th Electron. Components Technol. Conf., 2020, pp. 269–275, doi:10.1109/ECTC32862.2020.00052.

[32] M. Grujicic, C.L. Zhao, E.C. Dusel, The effect of thermal contact resistance on heat management in the electronic packaging, Appl. Surf. Sci. 246 (2005) 290–302, doi:10.1016/j.apsusc.2004.11.030.

[33] E.W. Lemmon, R.T. Jacobsen, Viscosity and Thermal Conductivity Equations for Nitrogen, Oxygen, Argon, and Air, Int. J. Thermophys. 25 (2004) 21–69, doi:10.1023/B:IJOT.0000022327.04529.f3.

[34] P. Swaminathan, M.D. Grapes, K. Woll, S.C. Barron, D.A. LaVan, T.P. Weihs, Studying exothermic reactions in the Ni-Al system at rapid heating rates using a nanocalorimeter, J. Appl. Phys. 113 (2013) 143509, doi:10.1063/1.4799628.

[35] A.S. Rogachev, S.G. Vadchenko, F. Baras, O. Politano, S. Rouvimov, N.V Sachkova, M.D. Grapes, T.P. Weihs, A.S. Mukasyan, Combustion in reactive multilayer Ni/Al nanofoils: Experiments and molecular dynamic simulation, Combust. Flame. 166 (2016) 158–169, doi:10.1016/j.combustflame.2016.01.014.

[36] I.E. Gunduz, K. Fadenberger, M. Kokonou, C. Rebholz, C.C. Doumanidis, T. Ando, Modeling of the self-propagating reactions of nickel and aluminum multilayered foils, J. Appl. Phys. 105 (2009) 74903, doi:10.1063/1.3091284.

[37] T.P. Weihs, 5 - Fabrication and characterization of reactive multilayer films and foils, in: K. Barmak, K. Coffey (Eds.), Met. Film. Electron. Opt. Magn. Appl., Woodhead Publishing, 2014, pp. 160–243, doi:10.1533/9780857096296.1.160.

[38] C.-S. Yoo, H. Wei, J.-Y. Chen, G. Shen, P. Chow, Y. Xiao, Time- and angle-resolved x-ray diffraction to probe structural and chemical evolution during Al-Ni intermetallic reactions, Rev. Sci. Instrum. 82 (2011) 113901, doi:10.1063/1.3658817.

[39] M.V Peralta-Martinez, W.A. Wakeham, Thermal Conductivity of Liquid Tin and Indium, Int. J. Thermophys. 22 (2001) 395–403, doi:10.1023/A:1010714612865.

[40] M.D. Wiemer, J. Braeuer, D. Wünsch, T. Gessner, Reactive Bonding and Low Temperature Bonding of Heterogeneous Materials, ECS Trans 33 (2019) 307–318, doi:10.1149/1.3483520.

[41] S.K. Kang, M.G. Cho, P. Lauro, D.-Y. Shih, Study of the undercooling of Pb-free, flip-chip solder bumps and in situ observation of solidification process, J. Mater. Res. 22 (2007) 557–560, doi:10.1557/jmr.2007.0071.

[42] Y. Huang, S. Chen, K. Wu, Size and Substrate Effects upon Undercooling of Pb-Free Solders, J. Electron. Mater. 39 (2010) 109–114, doi:10.1007/s11664-009-0966-1.

[43] W. Zhu, X. Wang, M. Li, Low-Temperature Bonding of Cu Through Self-Propagating Reaction Under Various Temperatures and Pressures, J. Electron. Packag. (2020) 142, doi:10.1115/1.4046341.

[44] S.M.L. Nai, J. Wei, M. Gupta, Improving the performance of lead-free solder reinforced with multi-walled carbon nanotubes, Mater. Sci. Eng. A. 423 (2006) 166–169, doi:10.1016/j.msea.2005.10.072.

[45] M.S.A. Karunaratne, S. Kyaw, A. Jones, R. Morrell, R.C. Thomson, Modelling the coefficient of thermal expansion in Ni-based superalloys and bond coatings, J. Mater. Sci. 51 (2016) 4213–4226, doi:10.1007/s10853-015-9554-3.

[46] J. Wang, E. Besnoin, A. Duckham, S.J. Spey, M.E. Reiss, O.M. Knio, M. Powers, M. Whitener, T.P. Weihs, Room-temperature soldering with nanostructured foils, Appl. Phys. Lett. 83 (2003) 3987–3989, doi:10.1063/1.1623943.